

Project: **620**

Project title: **Vertical Propagation of Gravity Waves into the Middle Atmosphere**

Project lead: **Andreas Dörnbrack**

Report period: **2020-01-01 to 2020-12-31**

In the reporting period, the computer time was mainly used to conduct simulations of deep mountain wave propagation events from the recently completed SOUTHTRAC-GW campaign (Rapp et al., 2020, Dörnbrack et al., 2020) and from the 2014 field campaign DEEPWAVE (Fritts et al., 2016). The results presented in the report for 2019 have been finally published (Bramberger et al., 2020, Gisinger et al., 2020, Wilms et al., 2020). Additionally, a few simulations have been run to support the publications by Englberger et al. (2020a, 2020b).

The new simulations for the ongoing project “Vertical Propagation of Gravity Waves into the Middle Atmosphere” are closely tied to the atmospheric conditions encountered during the field measurements of SOUTHTRAC-GW. This approach enables the interpretation of measurements by means of studying the dominant processes of gravity wave excitation and propagation. This brief report focuses on published results of 2D simulations of the flow over the Southern Andes to explain the occurrence of polar stratospheric clouds in El Calafate in in September 2019 (Dörnbrack et al., 2020). Furthermore, extended 3D numerical simulations have been conducted to explain the wave tunneling through the polar night jet leading to the ship-wave-like patterns that were observed directly above the Southern Ocean’s Auckland Islands but in about 87 km altitude. The reasons for these surprisingly deep vertical modes are here studied by newly conducted 3D simulations as planned in the previous year.

Unusual appearance of mother-of-pearl clouds above El Calafate, Argentina (50° 21’ S, 72° 16’ W)

Visual observations from the ground and from a glider soaring in the lowermost stratosphere revealed the existence of mother-of-pearl clouds above El Calafate, Argentina in the lee of the Andes on 11 September 2019. The lenticular shape of the observed clouds resembled polar stratospheric clouds (PSCs) frequently observed over the Scandinavian mountains. However, the altitude of the PSCs remained uncertain by these visual observations. Moreover, the appearance of the PSCs was rather unusual considering the time - end of the austral winter - and the location at about 50°S being far away from Antarctica. Fortunately, two nearby crossings by the German research aircraft HALO (High Altitude Long Duration research aircraft) show evidence that the PSCs were located at about 26 km altitude. This estimate is based on the enhanced backscatter signal of airborne lidar observations. In the paper by Dörnbrack et al. (2020), available observations are presented and the overall meteorological situation that was related to the earliest sudden stratospheric warming so far recorded in the Southern Hemisphere are described. By using high-resolution numerical simulations with EULAG we showed evidence of mountain waves propagating up to the stratosphere responsible for generating the localized cold stratospheric temperature anomalies required for PSC formation.



Figure 1: Mother-of-pearl clouds west, south-west of El Calafate on 11 September 2019. The picture was taken from outside the city at the cabins belonging to Brilllos Patagónicos, Calle 78 750, El Calafate (50.32°S, 72.26°W) at around 23 UTC. Photo taken by Marko Magister, Big Air Factory.



Figure 2: Snapshots of mother-of-pearl clouds from the camera installed at the Perlan 2 aircraft's tail wing. Left panel: position: 50.66°S, 73.04°W, altitude: 13873 m, true heading: 168.7°, time: 17:28:17 UTC. Right panel: position: 50.59°S, 73.04°W, altitude: 14933 m, true heading: 347.4°, time: 17:19:31 UTC.

Figure 1 presents a photograph of mother-of-pearl clouds that were taken from El Calafate at around 8 pm local time 11 September 2019 (23 UTC). During this day, strong surface winds prevailed and wave-induced cirrus clouds appeared over the Lago Argentino already in the morning.

The third deployment of the Airbus Perlan 2 mission¹ (Butler, 2016) took place in August/September 2019 in El Calafate. The manned glider Perlan 2 was designed to fly up to 90000 ft (FL 900). During the 2019 deployment, several flights were conducted reaching flight levels close to FL 500 (~ 15 km altitude) and one flight attaining FL 650 (~ 19.3 km on 16 September 2019). On 11 September 2019, Perlan 2 climbed up to FL 506 (15.2 km altitude at around 18 UTC). Before reaching the peak altitude, chief pilot Jim Payne spotted lenticular mother-of-pearl clouds in the stratosphere over the Andes at around 17:30 UTC. Figure 2 juxtaposes two snapshots from the tail wing camera of Perlan 2 displaying PSCs. Both photos were taken at nearly the same geographical location between 17:19 and 17:28 UTC. Obviously, the nearly 180° difference in the true headings of the glider indicates the existence of two spatially separated cloud groups, one group

¹ <https://perlanproject.org/> and <https://www.aerosociety.com/news/surfing-the-mountain-wave/>

located in south-west, the other north-west from the aircraft location. The northern group did not seem to persist as long into the evening as the southern group. A short movie from Perlan 2 soaring in the stratosphere and recording the mother-of-pearl clouds in the north-west can be found on the Perlan project page².

The numerical simulation were conducted in a computational domain extending 1260 km eastwards from 80°W and the model top is at 80 km altitude. The horizontal and vertical resolutions amount to 1 km and 500 m, respectively. The digital orography of the Andes along selected latitudes $\varphi = 50^\circ\text{S}$, 50.25°S , 50.50°S , 50.75°S , and 51°S is taken from ETOPO1 global relief model (Amante and Eakins, 2009) and interpolated onto the regular 1 km grid.

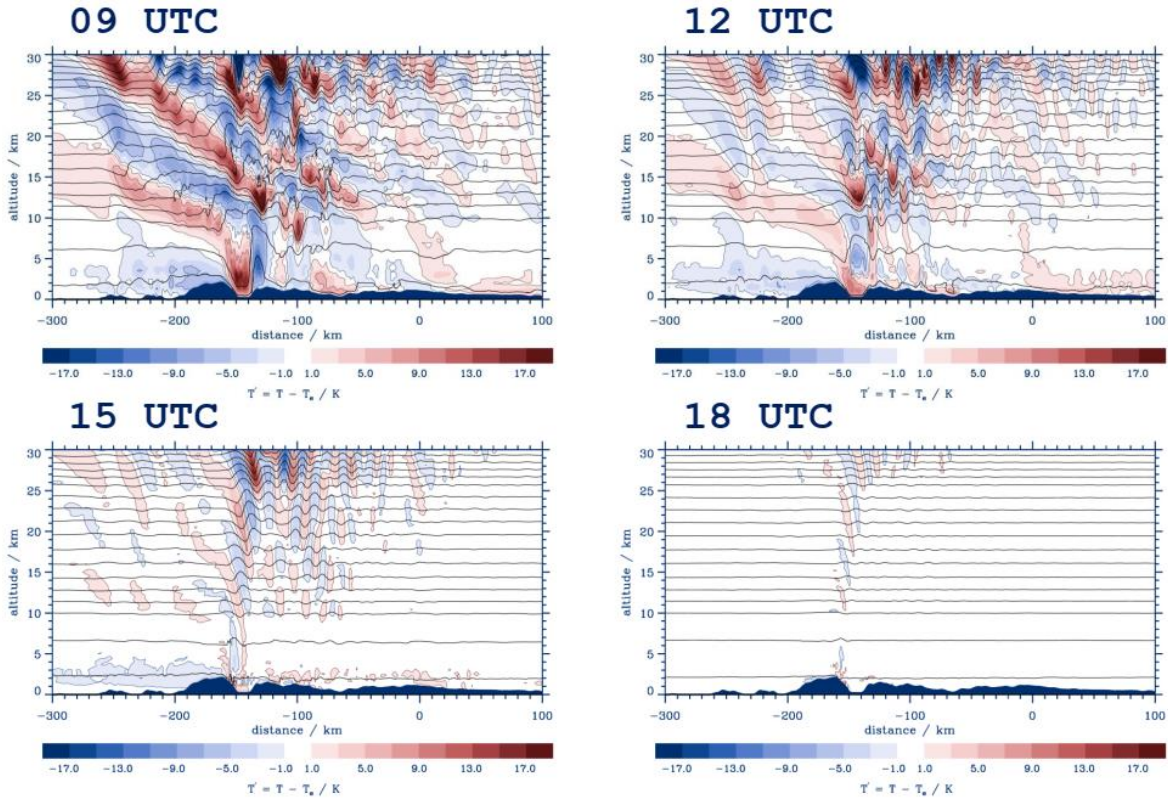


Figure 3: Temperature fluctuations $T - T_e$ (colour shaded, K) after 2 h simulation time from four EULAG simulations starting on 11 September 2019 at the given times. The orography is taken at $\varphi = 50^\circ\text{S}$.

The lower boundary is a material surface and we apply a free-slip boundary condition. As the main focus of the EULAG simulations was on the mountain wave response in the middle atmosphere we do not resolve the surface boundary layer. At the lateral edges of the computational domain open boundary conditions are imposed. Additionally, absorbing layers attenuate the flow variables toward their ambient states and avoid the reflection of waves into the computational domain. The sponge layers are 120 km wide and a relaxation time scale of 180 s was chosen. At the free-slip model top, $w = 0$ and we use a z -dependent relaxation in the whole domain mimicking the increasing dynamic viscosity with altitude, a method introduced by Prusa et al. (1996, Sec. 3b). This particular choice of a vertical sponge avoids the reflection of gravity waves from the model top. Background and initial fields are obtained from the ERA5 data set (Hersbach et al., 2020).

² <https://perlanproject.org/blog/perlan-2-soars-rare-stratospheric-perlan-clouds>

Simulations were performed using these ambient profiles as initial conditions in the whole domain.

The simulated mountain wave-induced temperature fluctuations $T' = T - T_e$ are shown in Figure 3 after 2 h simulation time. The four panels relate to different times of initialization ($t_{\text{INIT}} = 09, 12, 15,$ and 18 UTC) and ambient temperature profiles $T_e(z)$ correspond to the different initial profiles and do not change in time during the simulation. After 1 h simulation time all simulations show vertically propagating mountain waves. The T' -amplitudes are largest for the 09 and 12 UTC runs and they are nearly zero for the simulation starting at 18 UTC reflecting the reduced low-level forcing at this time. At about 25 km altitude T' falls below -10 K. After 2 h simulation time, the numerical simulations initialized at 09 and 12 UTC show strong nonlinearities resulting in overturning isentropic surfaces due to breaking mountain waves. The simulations using the later initialization times t_{INIT} remain nearly linear in the stratosphere due to the weaker low-level forcing. Amplitudes of T' maximize and T' attains values less than -10 K. This means, the stratospheric temperatures can be reduced by more than 10 K due to the adiabatic cooling in the ascending branches of the mountain waves. Given an ambient $T \sim 195$ K, local temperature below 185 K can be expected at around 25 km altitude appropriate for explaining the formation of the observed polar stratospheric cloud over El Calafate.

Deep Propagating Waves over Auckland Islands

Tyler Mixa has undertaken a reanalysis of a deep gravity wave propagation event observed over Auckland Island during the 2014 DEEPWAVE campaign (see Fritts et al., 2016). The initial observations (Pautet et al., 2016) indicated a gravity wave with a 40 km horizontal wavelength (λ_x) and temperature perturbations measured at ± 10 K at an altitude of 87 km (see Figure 4a). Eckermann et al. (2016) analysed this event using a linear Fourier ray model, using NAVGEM (Eckermann et al., 2018) reanalysis profiles of wind and temperature for altitudes up to 100 km (Fig. 4b) to reproduce the dominant gravity wave characteristics observed at 87 km (Fig. 4c), estimating the resulting gravity wave drag (GWD) of $300\text{-}600 \text{ m}^2 \text{ s}^{-2}$ at the GW breaking altitude.

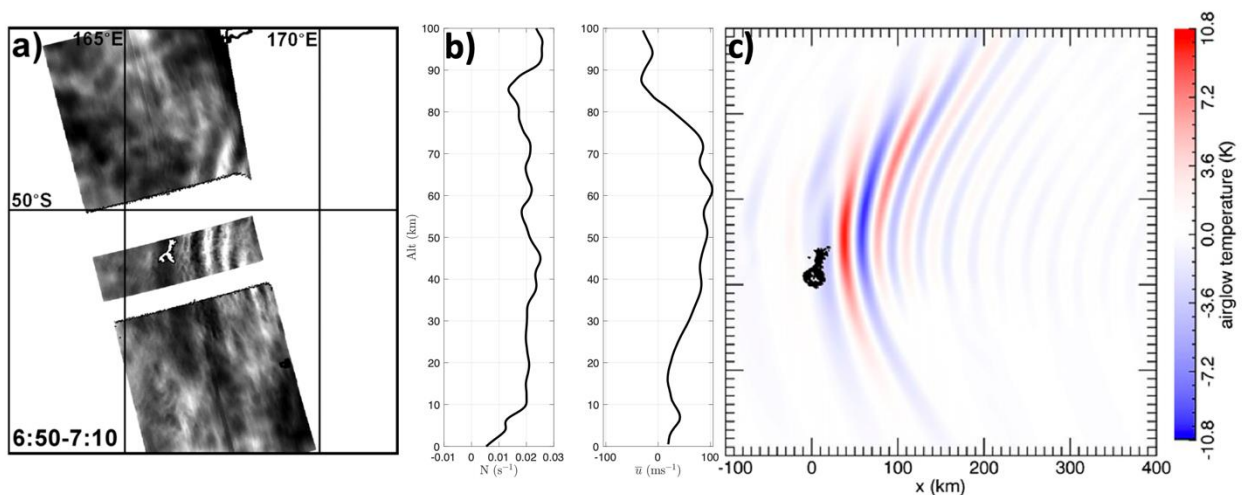


Figure 4: Initial AMTM GW observations from Pautet et al., 2016 at 87 km (a), NAVGEM vertical temperature and wind profiles (b), and simulation results from Eckermann et al., 2016 at 87 km (c).

The linear ray tracing model used by Eckermann et al. (2016) had several critical limitations motivating a reanalysis with EULAG. Linear ray propagation assumes a steady-state background atmosphere with

instantaneous gravity wave propagation from the source to the parameterized breaking altitude. The scheme traces individual ray paths from broad spectrum of gravity waves initialized at the ground and identifies the characteristics at 87 km based on the breaking altitude of each mode, with the approximate propagation time determined by each mode's vertical group velocity. As a linear model, this mechanism does not account for wave-wave interaction between different frequencies of gravity waves – gravity wave frequencies and wavelengths cannot change with space or time, all modes propagate independently of each other, and breaking altitudes are estimated with saturation amplitudes rather than fully characterized. Crucially, the results in Eckermann et al. (2016) removed gravity wave spectral components undergoing vertical reflections, resonance, and evanescent tunneling to evaluate purely propagating modes.

Description of Simulation Setup

For our numerical simulations, the 3D nonlinear compressible version of EULAG has been used to determine which propagation conditions enabling gravity wave penetration into the mesosphere and to elucidate how the resulting instability characteristics led to widespread momentum deposition. Results indicate that linear tunneling through the polar night jet (PNJ) enabled quick gravity wave propagation from the surface up to the mesopause. Subsequent instability processes reveal large mesospheric rolls that formed in the negative shear above the jet maximum and led to significant momentum deposition as they descended. Our study suggests that gravity wave tunneling is a viable source for this case and other deep propagation events reaching the mesosphere and lower thermosphere.

The simulations were conducted with the multiscale geophysical flow solver EULAG (Prusa et al., 2008, Smolarkiewicz et al., 2014). Here, the compressible Euler equations

$$\frac{d\mathbf{u}}{dt} = -c_p\theta\nabla\pi' - \mathbf{g}\frac{\theta'}{\theta_e} - \mathbf{f} \times \left(\mathbf{u} - \frac{\theta}{\theta_e}\mathbf{u}_e\right) - \alpha(\mathbf{u} - \mathbf{u}_e) + \mathbf{F}$$

$$\frac{d\theta'}{dt} = -\mathbf{u} \cdot \nabla\theta_e - \beta\theta'$$

$$\frac{d\rho}{dt} = -\rho\nabla \cdot \mathbf{u}$$

$$\pi = \left(\frac{R_d}{p_0}\rho\theta\right)^{R_d/c_v}$$

where $c_v = c_p - R_d$ are integrated numerically. In the above equations, the physical quantities have their usual meanings; primed quantities denote deviations to ambient states symbolized by subscript “e”. Although we solve for the Cartesian velocity $\mathbf{u} = (u, v, w)$, the operators d/dt , ∇ , $\nabla \cdot$ are formulated in generalized terrain-following coordinates (Prusa et al., 2003, Kühnlein et al., 2012). The above equations are integrated numerically as described by Smolarkiewicz et al. (2014).

The magnitude of the gravitational acceleration is given by $\mathbf{g} = (0, 0, -g)$. The Coriolis parameter is given as $\mathbf{f} \equiv 2\boldsymbol{\Omega}$, where $\boldsymbol{\Omega}$ denotes a constant angular velocity of the rotating reference frame. Equation 2 is written in perturbation form, i.e. $\theta' = \theta - \theta_e$, see Smolarkiewicz et al. (2019). In order to facilitate the numerical solution, these auxiliary ambient states, sometimes called environmental states (\mathbf{u}_e, θ_e) are assumed to be a

known particular solution of the above equations. In the paper by Mixa et al. (2020), only z -dependent profiles are prescribed that automatically satisfy the above equations. The terms involving $\alpha(\mathbf{x}, t)$ and $\beta(\mathbf{x}, t)$ represent forcings to attenuate the solution to the prescribed environmental profiles (\mathbf{u}_e, θ_e) . The forcing term $\mathbf{F} = (F_x, F_y, 0)$ in the momentum equations denotes an additional acceleration to ramp up the flow (see dashed and solid lines in Figure 2, Mixa et al., 2020).

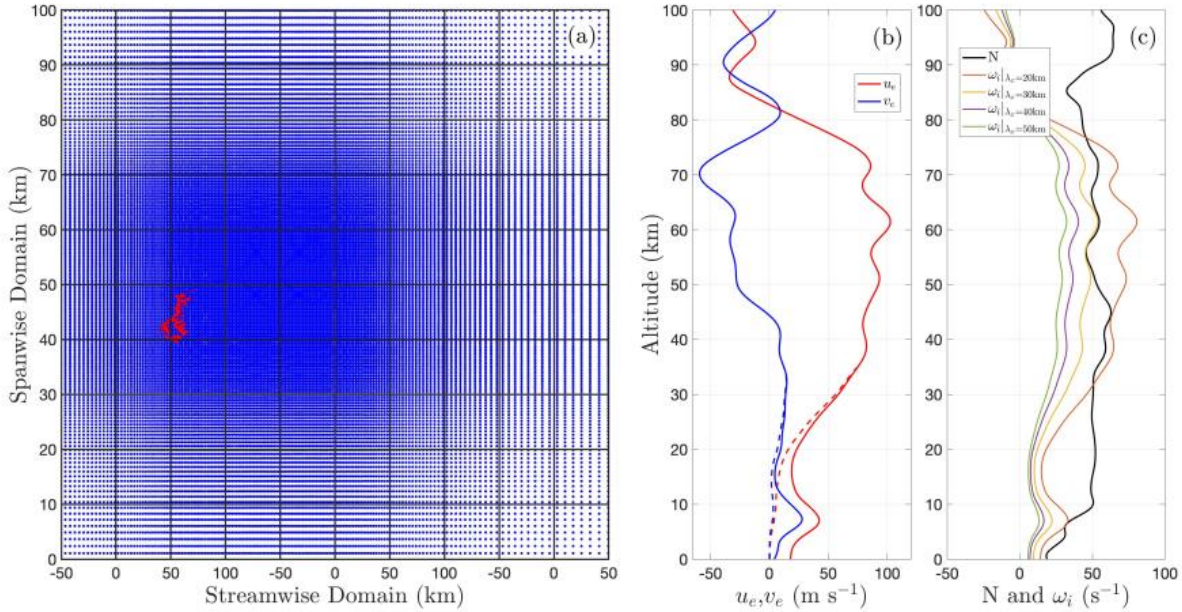


Figure 5: (a) Horizontal distribution of grid points in the computational domain. The red line marks the outlines of Auckland Island. (b) Vertical profiles of the ambient profiles u_e and v_e (solid lines), The dashed lines mark the respective initial profiles at $t=0$. The ramp-up of the low-level flow increases these values to the final values in a stepwise procedure. (c) Brunt-Väisälä frequency N and intrinsic frequency ω_i for selected values λ_x of stationary mountain waves.

Overview of Results

Three-dimensional nonlinear numerical simulations were conducted to investigate the vertical and horizontal propagation of internal gravity waves excited by the flow across Auckland Island up to the mesosphere. The numerical simulations reproduced the observed wave pattern in the OH airglow layer and attained corresponding horizontal wavelengths and temperature amplitudes (Figures 4 and 6). The inclusion of tunneling modes and full instability characterization augment previous findings for this event with several important takeaways, emphasizing that tunneling of non-hydrostatic mountain waves through an evanescent layer at the PNJ is the dominant process that enables quick penetration into the mesosphere, lower thermosphere (MLT). Crucially, tunneling gravity wave modes accelerate amplitude accrual above the PNJ and generate larger instabilities and a deeper gravity wave breaking region than estimated by Eckermann et al. (2016) and Pautet et al. (2016).

The three-dimensional numerical simulations revealed huge overturning vortices in the negative shear above the PNJ that propagated downward along the warm phases of the mountain waves. The vortical evolution of these “mesospheric rolls” represents a new class of instability morphology, following a characteristic sequence of events that defines the expected behavior for high frequency gravity waves breaking above the

PNJ. The resulting momentum deposition and gravity wave drag attain huge values (Figure 7) comparable to the values reported by various authors in recent papers and agree quantitatively with the estimates by Pautet et al. (2016) and Eckermann et al. (2006). Because the Auckland Island case produces such large sustained momentum fluxes from a “roughness mode”-scale topography source, there is a high likelihood that other small scale sources in the southern hemisphere could excite a similarly large response in the MLT.

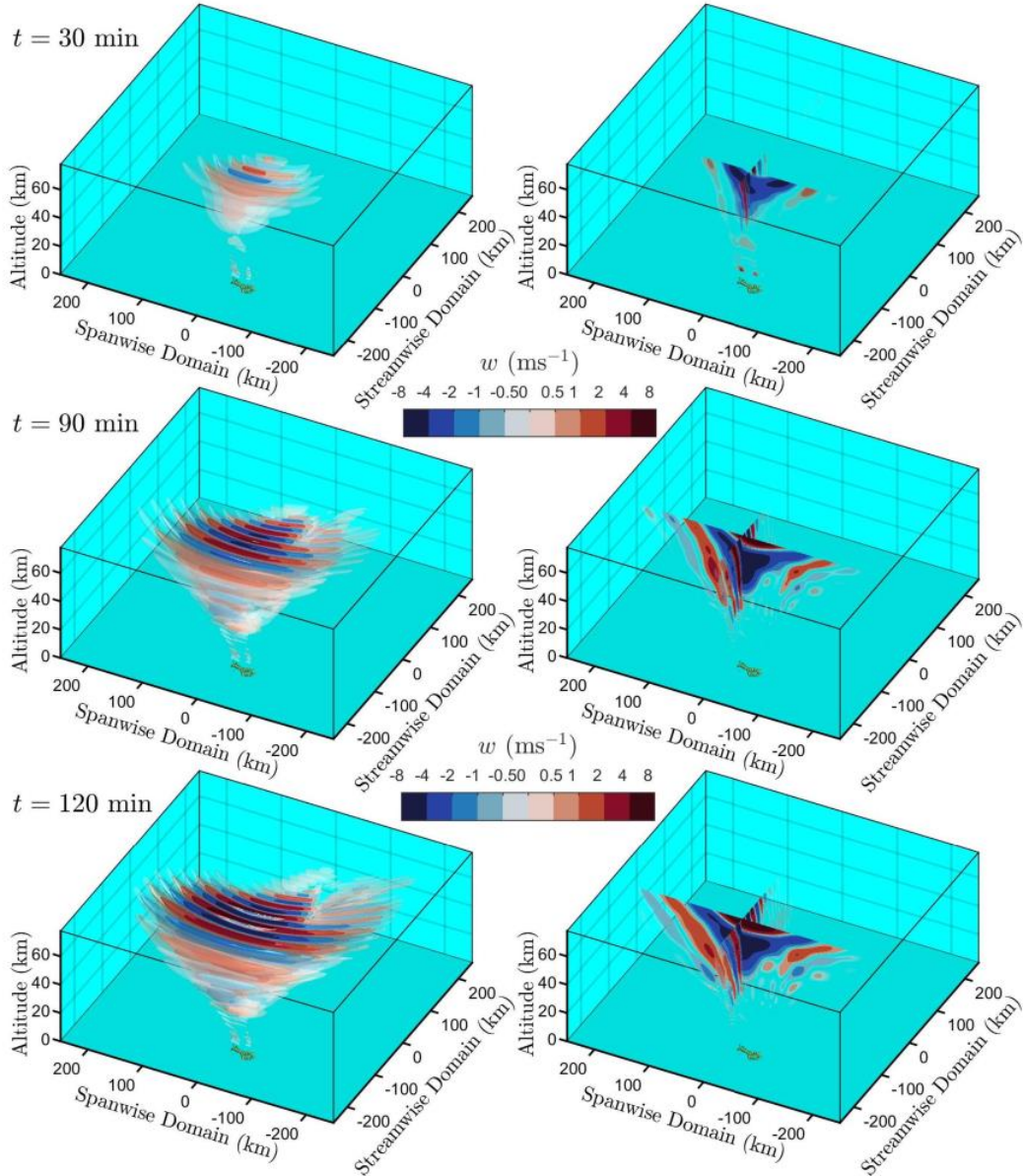


Figure 6: Time evolution of the simulated 3D vertical velocity field shown at elapsed times of 30 min (top), 90 min (middle), and 120 min (bottom). The 3D gravity wave phase structure is presented as both 1) a series of isosurfaces, plotted on a logarithmic scale with increasing opacity for higher values (left column); and 2) intersecting vertical slices through the domain at $(x,y)=(-130,-25)$ km for $t = 30$ min and $(x,y) = (-90,10)$ km for $t = 90$ min and $t = 120$ min (right column).

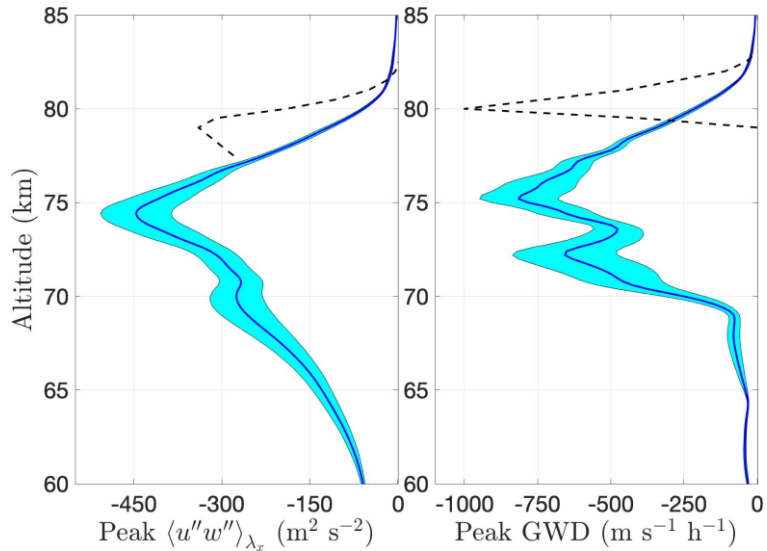


Figure 7: Time-averaged peak momentum flux per unit mass $\langle u''w'' \rangle$ and gravity wave drag (GWD) after the initial instability onset. Peak GWD occurs at a lower altitude than the theoretical level estimated by Eckermann et al. (2016) from linear saturation theory (shown in dashed black lines) because the vortical structures descend and expand over time.

Gravity wave tunneling enables small-scale tropospheric sources to have a significant impact on the MLT, contributing to faster gravity wave propagation that leads to amplitude accrual above the PNJ and rapid instability evolution which produces large regions of gravity wave drag. The long duration and extended latitude coverage of the PNJ suggest broad applicability of the propagation dynamics in this study to sub-Antarctic islands and other small-scale, mid-latitude gravity wave sources in the southern hemisphere. These subgrid-scale gravity wave modes have the potential to produce significant accumulated gravity wave drag in the southern hemisphere winter MLT. The continued absence of this MLT gravity wave drag source in global and mesoscale climate modeling suggests that addressing gravity wave tunneling dynamics is a viable approach to improve the accuracy of climate modeling in the southern hemisphere.

References (bold names are members of the project and the stars in front of the names mark this year's publications in the framework of the project))

Amante C. and B. W. Eakins, 2009: ETOPO1 1 Arc-Minute Global Relief Model: Procedures, Data Sources and Analysis. *NOAA Technical Memorandum NESDIS NGDC-24*. National Geophysical Data Center, NOAA. doi:10.7289/V5C8276M

* **Bramberger, M., A. Dörnbrack, H. Wilms**, F. Ewald, and R. Sharman, 2020: Mountain-Wave Turbulence Encounter of the Research Aircraft HALO above Iceland. *J. Appl. Meteor. Climatol.*, **59**, 567–588, <https://doi.org/10.1175/JAMC-D-19-0079.1>

Butler, D., 2016: Surfing glider set to study climate. *Nature* **536**: 134–135, (11 August 2016). doi:10.1038/536134a

* **Dörnbrack, A.**, Kaifler, B., Kaifler, N., Rapp, M., Wildmann, N., Garhammer, M., Ohlman, K., Payne, J., Sandercock, M., and E. Austin, 2020: Unusual appearance of mother-of-pearl clouds above El Calafate, Argentina (50° 21' S, 72° 16' W). *Weather*, in press.

Eckermann, S.D., D. Broutman, J. Ma, J.D. Doyle, P. Pautet, M.J. Taylor, K. Bossert, B.P. Williams, D.C. Fritts, and R.B. Smith, 2016: Dynamics of Orographic Gravity Waves Observed in the Mesosphere over the Auckland Islands during the Deep Propagating Gravity Wave Experiment (DEEPWAVE). *J. Atmos. Sci.*, **73**, 3855–3876.

Eckermann, S.D., J. Ma, K.W. Hoppel, D.D. Kuhl, D.R. Allen, J.A. Doyle, K.C. Viner, B.C. Ruston, N.L. Baker, S.D. Swadley, T.R. Whitcomb, C.A. Reynolds, L. Xu, N. Kaifler, B. Kaifler, I.M. Reid, D.J. Murphy, and P.T. Love, 2018: High-Altitude (0–100 km) Global Atmospheric Reanalysis System: Description and Application to the 2014 Austral Winter of the Deep Propagating Gravity Wave Experiment (DEEPWAVE). *Mon. Wea. Rev.*, **146**, 2639–2666.

* **Englberger, A.**, Lundquist, J. K., and **A. Dörnbrack**, 2020: Should wind turbines rotate in the opposite direction? *Wind Energ. Sci. Discuss.*, <https://doi.org/10.5194/wes-2019-105>. accepted 14 October 2020

* **Englberger, A., Dörnbrack, A.**, and Lundquist, J. K., 2020: Does the rotational direction of a wind turbine impact the wake in a stably stratified atmospheric boundary layer? *Wind Energ. Sci.*, **5**, 1359–1374, <https://doi.org/10.5194/wes-5-1359-2020>, 2020

Fritts, D.C., R.B. Smith, M.J. Taylor, J.D. Doyle, S.D. Eckermann, **A. Dörnbrack**, M. Rapp, B.P. Williams, P. Pautet, K. Bossert, N.R. Criddle, C.A. Reynolds, P.A. Reinecke, M. Uddstrom, M.J. Revell, R. Turner, B. Kaifler, J.S. Wagner, T. Mixa, C.G. Kruse, A.D. Nugent, C.D. Watson, **S. Gisinger**, S.M. Smith, R.S. Lieberman, B. Laughman, J.J. Moore, W.O. Brown, J.A. Haggerty, A. Rockwell, G.J. Stossmeister, S.F. Williams, G. Hernandez, D.J. Murphy, A.R. Klekociuk, I.M. Reid, and J. Ma, 2016: The Deep Propagating Gravity Wave Experiment (DEEPWAVE): An Airborne and Ground-Based Exploration of Gravity Wave Propagation and Effects from Their Sources throughout the Lower and Middle Atmosphere. *Bull. Amer. Meteor. Soc.*, **97**, 425–453.

* **Gisinger, S.**, Wagner, J., and Witschas, B.: Airborne measurements and large-eddy simulations of small-scale gravity waves at the tropopause inversion layer over Scandinavia, *Atmos. Chem. Phys.*, **20**, 10091–10109, <https://doi.org/10.5194/acp-20-10091-2020>, 2020.

Hersbach, H, Bell, B, Berrisford, P, *et al.*, 2020: The ERA5 global reanalysis. *Q J R Meteorol Soc.* 146: 1999– 2049. <https://doi.org/10.1002/qj.3803>

Kühnlein C., Smolarkiewicz P. K., **Dörnbrack A.**, 2012: Modelling atmospheric flows with adaptive moving meshes. *J. Comput. Phys.* 231: 2741–2763.

* **Mixa, T., A. Dörnbrack**, and M. Rapp, 2020: Nonlinear Simulations of Gravity Wave Tunneling and Breaking over Auckland Island, *J. Atmos. Sci.*, under revision.

Pautet, P.-D., Taylor, M. J., Fritts, D. C., Bossert, K., Williams, B. P., Broutman, D., Ma, J., Eckermann, S. D., and Doyle, J. D. (2016), Large-amplitude mesospheric response to an orographic wave generated over the Southern Ocean Auckland Islands (50.7°S) during the DEEPWAVE project, *J. Geophys. Res. Atmos.*, 121, 1431–1441.

Prusa J. M., Smolarkiewicz P.K. and R. R. Garcia, 1996: Propagation and Breaking at High Altitudes of Gravity Waves Excited by Tropospheric Forcing. *J. Atmos. Sci.* 53: 2186–2216. [https://doi.org/10.1175/1520-0469\(1996\)053<2186:PABAHA>2.0.CO;2](https://doi.org/10.1175/1520-0469(1996)053<2186:PABAHA>2.0.CO;2)

Prusa J. M. and P. K. Smolarkiewicz, 2003: An all-scale anelastic model for geophysical flows: dynamic grid deformation. *J. Comput. Phys.* 190: 601–622.

Prusa J. M., P. K. Smolarkiewicz and A. A. Wyszogrodzki, 2008: EULAG, a computational model for multiscale flows. *Comput. Fluids* 37: 1193–1207.

*Rapp, M., B. Kaifler, **A. Dörnbrack**, **S. Gisinger**, **T. Mixa**, R. Reichert, N. Kaifler, S. Knobloch, R. Eckert, N. Wildmann, A. Giez, L. Krasauskas, P. Preusse, M. Geldenhuys, W. Woiwode, F. Friedl-Vallon, B.-M. Sinnhuber, A. de la Torre, P. Alexander, J. L. Hormaechea, D. Janches, M. Garhammer, J. L. Chau, J. F. Conte, P. Hoor, and A. Engel, 2020: SOUTHTRAC-GW: An airborne field campaign to explore gravity wave dynamics at the world's strongest hotspot. *Bull. Americ. Met. Soc.*, under revision.

Smolarkiewicz P. K., C. Kühnlein, and N. P. Wedi, 2014: A consistent framework for discrete integrations of soundproof and compressible PDEs of atmospheric dynamics. *J. Comput. Phys.* 263: 185–205. <https://doi.org/10.1016/j.jcp.2014.01.031>

***Wilms, H., Bramberger, M., and A. Dörnbrack**, 2020: Observation and Simulation of Mountain Wave Turbulence above Iceland: Turbulence Intensification due to Wave Interference. *Q. J. R. Met. Soc.*, 1–21. <https://doi.org/10.1002/qj.3848>